Design and Control of a 3 kW Wireless Power Transfer System for Electric Vehicles

Zhenshi Wang [1,2], Xuezhe Wei [2,*] and Haifeng Dai [1,2]

[1] Clean Energy Automotive Engineering Center, Tongji University, No. 4800, Caoan Road, Shanghai 201804, China; 1022wangzhenshi@tongji.edu.cn
[2] School of Automotive Studies, Tongji University, No. 4800, Caoan Road, Shanghai 201804, China; tongjidai@tongji.edu.cn
* Correspondence: weixzh@tongji.edu.cn; Tel.: +86-135-0184-8129

Abstract: This paper aims to study a 3 kW wireless power transfer system for electric vehicles. First, the LCL-LCL topology and LC-LC series topology are analyzed, and their transfer efficiencies under the same transfer power are compared. The LC-LC series topology is validated to be more efficient than the LCL-LCL topology and thus is more suitable for the system design. Then a novel q-Zsource-based online power regulation method which employs a unique impedance network (two pairs of inductors and capacitors) to couple the cascaded H Bridge to the power source is proposed. By controlling the shoot-through state of the H Bridge, the charging current can be adjusted, and hence, transfer power. Finally, a prototype is implemented, which can transfer 3 kW wirelessly with ~95% efficiency over a 20 cm transfer distance.

1. Introduction

Research on wireless power transfer began soon thereafter the famous Tesla coils were invented by Nikola Tesla in 1889 [1,2], and many good results have been achieved [3–6]. In 2007, researchers at MIT proposed strongly coupled magnetic resonances (SCMR), by which they were able to transfer 60 watts wirelessly with ~40% efficiency over distances in excess of 2 m [7]. Various research hot spots, including system architectures, optimization design, frequency splitting, impedance matching and special applications, have been investigated [8–14]. Wireless power transfer is very suitable for charging electric vehicles [15–17], as it can avoid the troublesome plug-in process, provide an inherent electrical isolation and adapt to harsh environments. However, SCMR is not appropriate for automotive applications, as its operating frequency is very high, which goes beyond the limitation of SAE J2954 (work in progress). As another kind of wireless power transfer techniques, inductive power transfer (IPT) has developed for more than twenty years [5], and it mainly focuses on the high power level applications, where the issues of concern normally include power conversion and control [18,19], magnetic structure design [20], control algorithm and strategy [21,22] as well as circuit topology [23]. Basically, both SCMR and IPT conforms to Faraday's and Ampere's laws, and their differences primarily include the design approaches, system architectures, parameter selection and transfer characteristics [6,24].

This paper aims to study a 3 kW vehicle-mounted wireless power transfer system, on which two key parts, the resonant topology analysis and comparison, and the online power regulation, are elaborated. Many resonant topologies are available for wireless power transfer system, but the most basic ones are only series-series, series-parallel, parallel-series and parallel-parallel [23], and the

others are all derived from these ones. A wireless power transfer system for electric vehicles requires a resonant topology that should have a unity-power-factor and a current source characteristic [18], no matter whether the distance or angle between the chassis and the ground changes or not. In this paper the characteristics of the LC-LC series and LCL-LCL topologies are analyzed first, and we prove that they both have the required unity-power-factor and current source characteristics. Then the transfer efficiencies of the LC-LC series and LCL-LCL topologies are compared under the same transfer power conditions, and the comparison results validate that the LC-LC series topology is more suitable for the system design due to its higher transfer efficiency. In practice, the distance or angle between vehicle chassis and ground often changes [25], as drivers cannot park their cars at the same location every time, and naturally, online power regulation is indispensable in the battery charging process. Traditional power regulation methods include cascade DC/DC, dead time modulation and phase shifting control [26]. However, the cascade DC/DC may increase the number of devices, decrease the power density and lower the transfer efficiency, while dead time modulation may distort the output waves produced by the H Bridge, and the phase shifting control cannot boost the transfer power, so a novel q-Zsource-based power regulation method is proposed in this paper, which employs two pairs of inductors and capacitors as a unique boost network. The power regulation is realized by controlling the shoot-through state of the H Bridge, and there are no extra power switch devices. By combining the phase shifting control and shoot-through state control, the square-wave voltage produced by the H Bridge can be adjusted arbitrarily, and hence, the transfer power.

2. Comparative Analysis of Resonant Topologies

2.1. LC-LC Series Topology

Wireless power transfer systems normally consist of a power source, a H Bridge, a resonant topology, a rectifier as well as a load. With the classical frequency-domain analysis, we can easily get the amplitude-frequency characteristics of resonant topologies, which are steep spikes, and the maximal point just emerges at the resonant frequency. For example, the LC-LC series topology has a four order transfer function, and the LCL-LCL topology has a six order transfer function. These two resonant topologies only allow the fundamental components of the square-wave voltages produced by the H Bridge to pass through, thus the resonant topology input can be substituted by a quasi-sine voltage source. As the power batteries have strong voltage source characteristics, the rectifier and battery pack can be also simplified into a quasi-sine voltage source, the amplitude of which depends on the battery pack voltage multiplied by $4/\pi$. The simplified LC-LC topology [27,28] is shown in Figure 1.
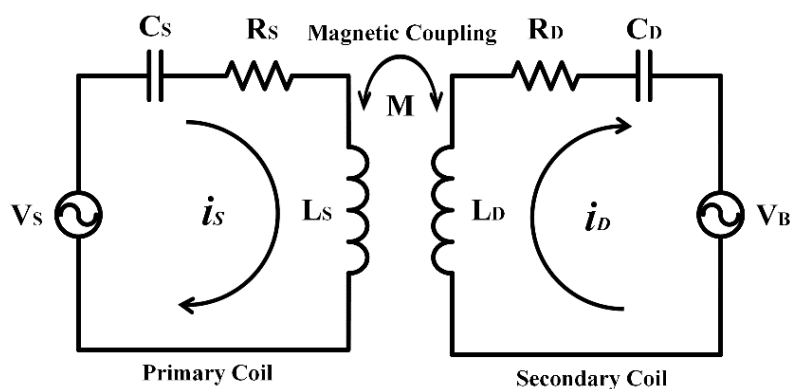

Figure 1. LC-LC series topology.

In Figure 1, L_S and L_D represent the magnetic coils, C_S and C_D represent the resonant capacitors, R_S and R_D represent the parasitic resistances, and M is the mutual inductance between L_S and L_D. When the system works in the resonant state, one has:

$$\begin{cases} V_S = i_S R_S - j\omega_r M i_D \\ j\omega_r M i_S = i_D R_D + j V_B \end{cases} \tag{1}$$

where i_S and i_D are the resonant currents in the primary and secondary coils, and ω_r is the system resonant frequency. By solving Equation (1), we have:

$$\begin{cases} |i_S| = \dfrac{V_S + \dfrac{\omega_r M V_B}{R_D}}{R_S + \dfrac{(\omega_r M)^2}{R_D}} \\ |i_D| = \dfrac{\dfrac{\omega_r M V_S}{R_S} - V_B}{R_D + \dfrac{(\omega_r M)^2}{R_S}} \end{cases} \tag{2}$$

Equation (2) shows that the charging current i_D depends on $\omega_r, M, R_S, R_D, V_S$ and V_B. Normally, V_B may change while charging, as it increases with the state of charge (SOC) of the battery. Because $\omega_r = 2\pi f_r$ is up to 100 kHz, M is from 20 μH to 100 μH, R_S is in the milliohm level, and V_S is usually larger than V_B, we have:

$$\frac{\omega_r M V_S}{R_S} \gg V_B \tag{3}$$

By substituting Equation (3) into Equation (2), we can find that i_D remains unchanged during the whole charging process, which realizes a constant-current charging function. As the product of R_S and R_D is smaller than either of them, Equation (2) is further simplified into:

$$\begin{cases} |i_S| = \dfrac{V_B}{\omega_r M} \\ |i_D| = \dfrac{V_S}{\omega_r M} \end{cases} \tag{4}$$

It is worth mentioning that the current source characteristic of LC-LC series topology is tenable only when the charging objects are batteries or some other capacitive load. Based on Equation (2), the transfer power can be expressed as:

$$P_{LC-LC} = |i_D| \cdot V_B = \frac{\omega_r M V_S - V_B R_S}{R_D R_S + \omega_r{}^2 M^2} \cdot V_B \tag{5}$$

2.2. LCL-LCL Topology

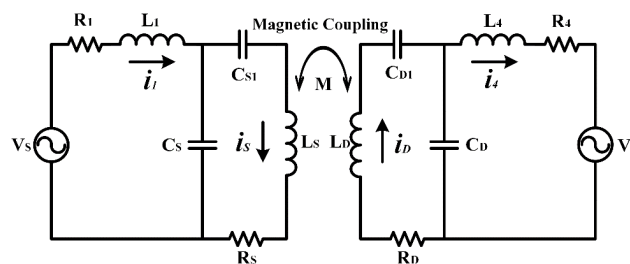Similarly, the simplified LCL-LCL topology [18,29–31] is shown in Figure 2.

Figure 2. LCL-LCL topology.

In this figure, L_1 and L_4 are the matching inductors of L_S and L_D, R_1 and R_4 are their parasitic resistances. For high power applications, L_S and L_D are normally bulky, which make L_1 and L_4 bulky, and this is not beneficial for the objectives of miniaturization and lightness. Thus the compensating capacitors C_{S1} and C_{D1} are introduced to decrease L_1 and L_4. Still, they should satisfy the following equations:

$$C_{S1} = \frac{1}{\omega_r^2(L_S - L_1)}, \ C_{D1} = \frac{1}{\omega_r^2(L_D - L_4)} \tag{6}$$

$$\omega_r = \frac{1}{\sqrt{L_1 C_S}} = \frac{1}{\sqrt{L_4 C_D}} \tag{7}$$

Actually, LCL is a transformation of the LC parallel topology [18]. It is well-known that the reflected impedance of the LC parallel topology contains an imaginary part [23], especially when the mutual inductance and the load change online, which makes the tuning process very cumbersome. The additional inductor of the LCL topology can just eliminate this imaginary part whether the mutual inductance and the load change or not. Using a method similar to that in Section 2.1, we can conclude that the LCL-LCL topology also has constant-current charging characteristics. The parasitic resistances are usually small due to the use of Litz wires, thus neglecting the parasitic resistances will not affect the system efficiency sharply, and in practice that loss is very small compared with the loss caused by the H Bridge and rectifier, so we can get the simplified calculation formulas of the LCL-LCL topology as follows:

$$i_S = \frac{V_S}{j\omega_r L_1}, \ i_4 = j\frac{MV_S}{\omega_r L_1 L_4}, \ i_D = \frac{V_B}{j\omega_r L_4}, \ i_1 = j\frac{MV_B}{\omega_r L_1 L_4} \tag{8}$$

The transfer power can be written as:

$$P_{LCL-LCL} = \frac{MV_S V_B}{2\omega_r L_1 L_4} \tag{9}$$

Equation (9) shows that the charging power can be adjusted by V_S. Unlike Equation (5), there are two additional power regulation freedoms L_1 and L_4.

2.3. Comparison between the LC-LC Series Topology and LCL-LCL Topology

The LC-LC series topology and LCL-LCL topology are widely used in practice, as both can realize the constant-current charging characteristics, the unity-power-factor characteristics and even bidirectional power transfer characteristics. Their transfer power characteristics are however different, for instance, the transfer power of the LC-LC series topology increases with the increasing transfer distances according to Equation (5), and the transfer power of the LCL-LCL topology decreases with the increasing transfer distance according to Equation (9). However, their transfer efficiency characteristics have not been compared before, thus this section aims to compare them to provide some suggestions for practical engineering design. The charging power and magnetic coils of the two topologies must be identical, as only then can the efficiency comparison be meaningful. The charging power of the LC-LC series topology equals to that of LCL-LCL topology, if their charging currents are designed to be the same, as they both have the constant-current characteristic. Based on Equations (4) and (8), we can write:

$$\frac{V_S}{\omega_r M} = \frac{MV_S}{\omega_r L_1 L_4} \tag{10}$$

From Equation (10), one has $M^2 = L_1 L_4$. This means that the charging power of the two topologies are the same if the product of two compensating inductors in the LCL-LCL topology equals the mutual inductance M. When the transfer distances are 10, 15, 20, 25 and 30 cm, the measured mutual inductances between two magnetic coils (L_S and L_D) are 107.155 μH, 66.66 μH, 42.538 μH, 28.125 μH, 18.888 μH, respectively. Normally, the distance between the chassis and ground is around 20 cm, thus
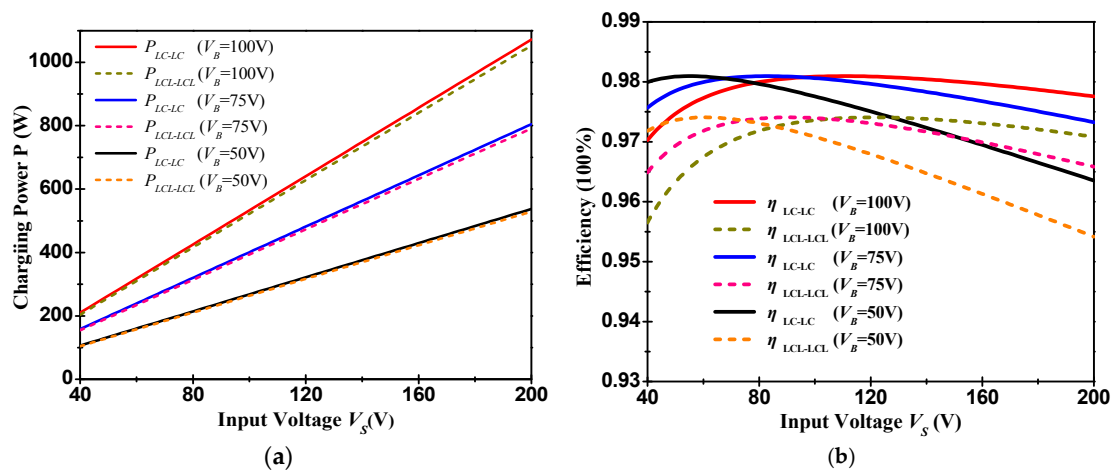
the corresponding mutual inductance M is around 42.538 μH. Assuming that L_1 equals L_4, one has $L_1 = L_4 = 42.538$ μH. Because the magnetic coils of the LCL-LCL topology are the same as those of the LC-LC series topology, the electric parameters of the LC-LC series topology and LCL-LCL topology can be summarized as shown in Table 1.

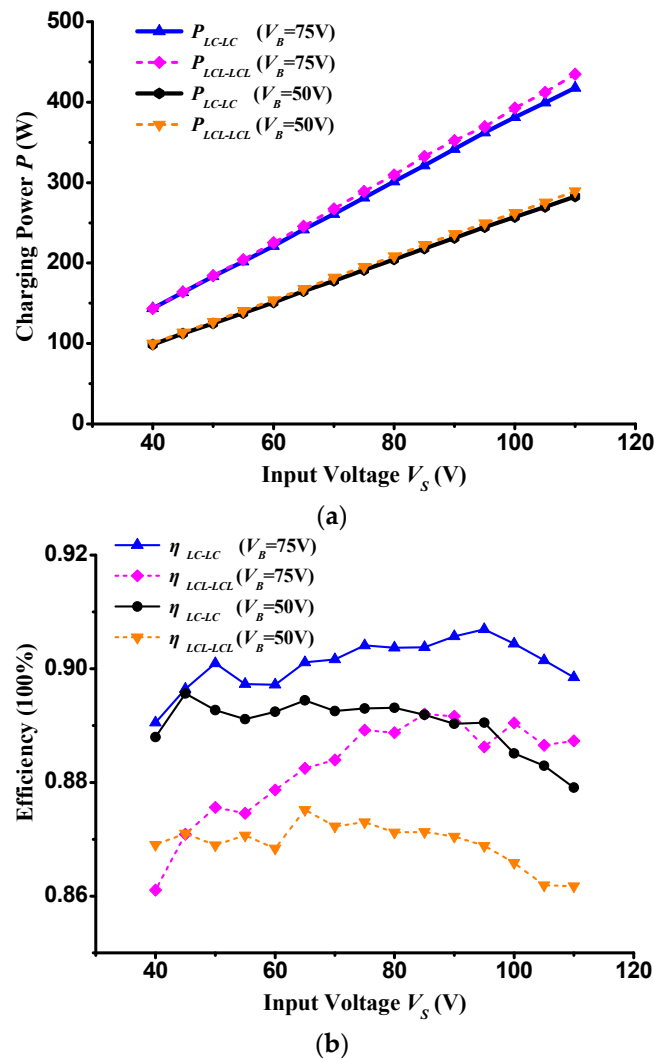**Table 1.** Detailed parameters of the LC-LC series topology and LCL-LCL topology.

LC-LC Series Topology		LCL-LCL Topology	
Electric parameters	Value	Electric parameters	Value
Primary inductor L_S	290.18 μH	Compensating inductor L_1	43.2 μH
Parasitic resistance R_S	193 mΩ	Parasitic resistance R_1	53 mΩ
Primary capacitor C_S	34.83 nF	Primary resonant capacitor C_S	234.75 nF
Secondary inductor L_D	329.4 μH	Primary inductor L_S	290.18 μH
Parasitic resistance R_D	213 mΩ	Parasitic resistance R_S	193 mΩ
Secondary capacitor C_D	30.89 nF	Compensating capacitor C_{S1}	40.68 nF
		Secondary inductor L_D	329.4 μH
		Parasitic resistance R_D	213 mΩ
		Compensating capacitor C_{D1}	35.07 nF
		Compensating inductor L_4	42.5 μH
		Parasitic resistance R_4	42.5 mΩ
		Secondary resonant capacitor C_D	238.63 nF

The detailed efficiency expressions of LC-LC topology and LCL-LCL topology are given by references [27,30–32], and can be also deduced using Maple. Then we substitute the data of Table 1 into the power and efficiency expressions of the LC-LC series and LCL-LCL topologies, and their resulting transfer characteristics are as shown in Figure 3.

Figure 3a shows that the charging power of these two topologies are the same, despite the different battery voltages, and Figure 3b shows that the efficiency of the LC-LC series topology is higher than that of the LCL-LCL topology. Note that the theoretical results ignore the losses caused by the H Bridge and rectifier, so the efficiency losses are mainly due to the parasitic resistances of the inductors and capacitors. The parasitic resistances of compensating capacitors are usually ignored, for they are far smaller than those of magnetic coils. Compared with the LC-LC series topology, the LCL-LCL topology has another two compensating inductors, the parasitic resistances of which further cause a drop in the transfer efficiency. In order to verify the correctness of theoretical calculations, the experiments are performed, and the results are shown in Figure 4.

Figure 3. Theoretical transfer power (**a**) and efficiencies (**b**) of the LC-LC series and LCL-LCL topologies.

Figure 4. Experimental transfer power (**a**) and efficiencies (**b**) of the LC-LC series and LCL-LCL topologies.

The results in Figure 4a show a good agreement with those in Figure 3a. However, the experimental transfer efficiencies decline sharply compared with those in Figure 3b, which is mainly because the H Bridge and rectifier introduce additional losses. Still, it is obvious that the efficiency of the LC-LC series topology is superior to that of the LCL-LCL topology, so this paper adopts the LC-LC series topology as the power transfer carrier.

3. Online Power Regulation

3.1. Principles of q-Zsource

Z-source is a unique impedance network with two pairs of inductors and capacitors connected in an X shape [33] as shown in Figure 5a, and it was initially used for stabilizing the widely changing voltage produced by fuel cell stacks. Compared with the Z-source, the q-Zsource shown in Figure 5b has better performance [34]. The most obvious two virtues are as follows: first, there is an input inductor L_1, which enables the input current to be continuous and thus limits the transient peak loss. Second, the withstand voltage for C_1 is lowered, for C_1 always combines with power source to charge or discharge L_1. This allows the volume and weight of C_1 to be reduced, and improves system power density.
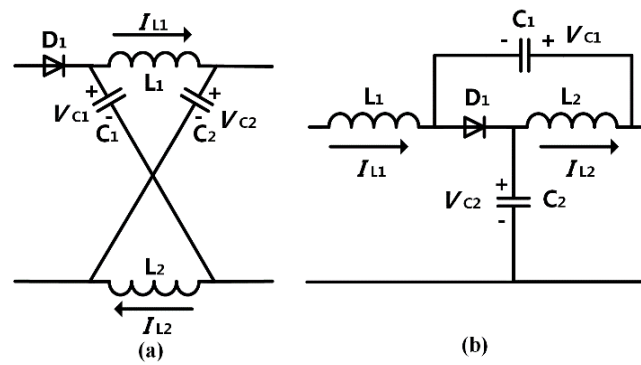
Figure 5. Topologies of Z-source (**a**) and q-Zsource (**b**).

This paper introduces the q-Zsource, not for stabilizing the output, but to produce a changeable output voltage, which can adjust the charging current, and hence, the charging power. The overall system schematic is depicted in Figure 6.
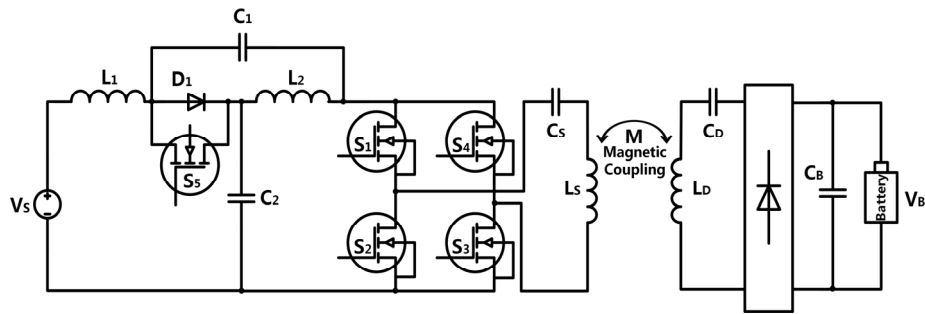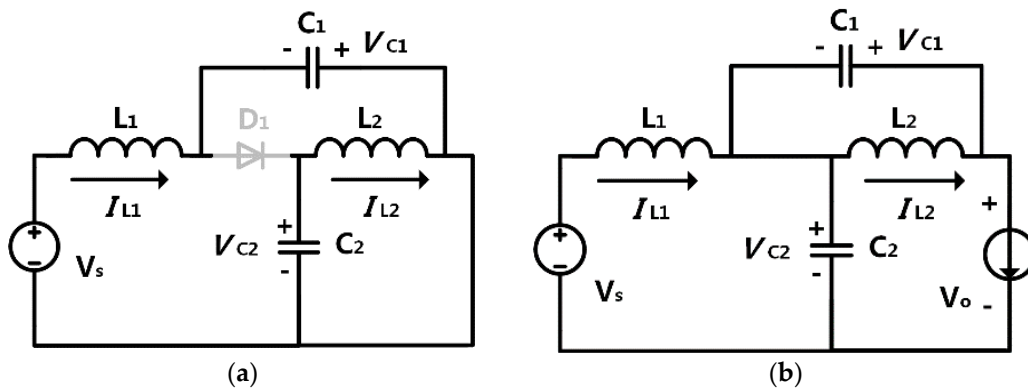

Figure 6. Overall schematic of the wireless power transfer system.

It clearly shows that the whole system consists of the power source, the q-Zsource, the H Bridge, the primary and secondary resonators, the rectifier, the filter and the battery pack. Unlike other system structures, the q-Zsource between the power source and H Bridge is first employed to boost the wireless charging power. By controlling the shoot-through state of the H Bridge, the input voltage to the H Bridge can be boosted through the q-Zsource, so the transmitter current can be adjusted, and hence, the charging current and power for the battery pack. Compared with some typical primary unit current control methods [35], the proposed method has two major merits: first, the digital control of the q-Zsource can be integrated into the primary microprocessor, and there are no active power switches in the proposed method, which can lower the system cost. Secondly, all the current or power regulation devices are included in the primary unit, and this design is beneficial to the vehicle miniaturization and lightness, as the secondary unit can be small and light. There is an additional MOSFET, S_5, connected in parallel with D_1 in Figure 6, and it is used to avoid discontinuous operation conditions when the load is light. To further demonstrate it, assume that there is a light load and the q-Zsource only consists of D_1. The diode D_1 will turn off when the current flowing through it decreases to zero, thus the connection between the q-Zsource and power source is disconnected, and the relationship between them will not be tenable. This abnormal state makes the output voltage of q-Zsource change freely, and further induces a decline of the system transfer characteristics. This unwanted phenomenon will disappear if S_5 is turned on or off actively. S_5 can be also removed if the system always works at the rated state. The q-Zsource has two typical operating states, and the equivalent circuits are depicted in Figure 7.

Figure 7. Equivalent circuits of q-Zsource in shoot-through state (**a**) and non-shoot-through state (**b**).

The operating mode of the q-Zsource is controlled by the cascade H Bridge. When the H Bridge works in the traditional phase shifting state, no voltage boosting phenomenon happens, but when the system charging power needs to be increased, making either of the bridge arms to be shoot-through, the voltage boosting phenomenon happens. The output of the q-Zsource is shorted by the H Bridge in the shoot-through state, and L_2 is charged by C_2, L_1 is charged by C_1 and V_S, whereas the H Bridge becomes an equivalent current source in the non-shoot-through state as shown in Figure 7b, C_2 and L_2 provide the output voltage together, C_1, L_1 and V_S provide the output voltage together. This also explains why the withstand voltage across C_1 reduces. By controlling the ratio between shoot-through time and non-shoot-through time, the output voltage of the q-Zsource can be adjusted. From Figure 7a, we have:

$$V_S + V_{C1} = V_{L1}, \; V_{C2} = V_{L2} \tag{11}$$

Similarly, from Figure 7b, we have:

$$V_S + V_{L1} + V_{C1} = V_O, \; V_S + V_{L1} = V_{C2}, \; V_{C1} = V_{L2}, \; V_{C1} + V_{C2} = V_O \tag{12}$$

Normally, L_1 equals L_2, and the currents flowing through them are the same, thus one has:

$$V_{L1} = V_{L2} \tag{13}$$

Since the volt-seconds of the inductor should be identical in the steady state, we can get:

$$(V_{C1} + V_S) \cdot T_S = (V_O - V_{C1} - V_S) \cdot T_N \tag{14}$$

T_S represents the shoot-through time and T_N represents the non-shoot-through time, the sum of those is the whole cycle time T. Then substituting Equations (11)–(13) into Equation (14), we have:

$$V_O = \frac{T}{T_N - T_S} \cdot V_S = \frac{1}{1 - 2D} \cdot V_S = BF \cdot V_S \tag{15}$$

$D = T_S/T$ is the duty cycle, BF is the boost factor produced by the shoot-through state, and it is always greater than or equal to 1. Additionally, we can also obtain the voltages across the capacitor C_1 and C_2:

$$V_{C1} = \frac{V_O - V_S}{2} = \frac{T_S}{T_N - T_S} \cdot V_S = \frac{D}{1 - 2D} \cdot V_S \tag{16}$$

$$V_{C2} = \frac{V_O + V_S}{2} = \frac{T_N}{T_N - T_S} \cdot V_S = \frac{1 - D}{1 - 2D} \cdot V_S \tag{17}$$

3.2. Control Method

Unlike the traditional buck or boost converter, the duty cycle *D* of the q-Zsource cannot reach 50% according to Equation (15). The voltage gain curve of the q-Zsource is shown in Figure 8, and it clearly shows that there are two operating regions.
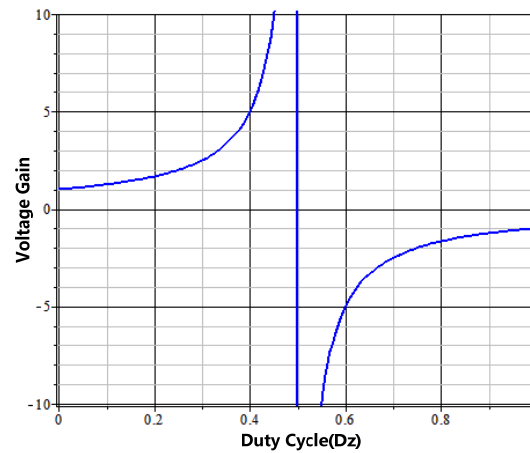

Figure 8. Voltage gain of the q-Zsource.

When *D* is greater than 0.5, the q-Zsource enters the negative gain region, and produces a negative output voltage, which is hardly used in practice. When *D* is less than 0.5, it produces a positive output voltage, thus we should limit the duty cycle *D* to below 0.5. All the traditional control strategies [26] can be used to control the q-Zsource and their theoretical input-output relationships still hold, the only difference is that the shoot-through time is added. The traditional phase shifting control is widely used to produce the square-wave voltages and realize the soft-switching conditions. However, it will not be discussed in this paper, as this control method has already been explained before [36]. It is worth mentioning that the q-Zsource has no effect on the output waves of the H Bridge in this mode, and only acts as a kind of filter.

When the charging power needs to be boosted, the H Bridge enters the new operating mode shown in Figure 9, which supplies the shoot-through state for the q-Zsource to boost the output voltage. Unlike the traditional phase shifting control, an additional shoot-through time $T_{shoot-through}$ is added into the control sequences, The dead time T_{dead}, shifting time $T_{shifting}$ and shoot-through time $T_{shoot-through}$ influence the output waves together. The shoot-through state in Figure 9 is realized by turning on S_3 and S_4 simultaneously, or it can be also realized by simultaneously turning on S_1 and S_2, which depends on the practical situations. The interval between t_0 and t_7 is the whole control cycle, as it is symmetrical, only the operating mode among $t_0 \sim t_3$ needs to be demonstrated. S_1 is turned off at t_0, while I_H is still positive, thus it is forced to flow through the free-wheeling diode of S_2. Before I_H changes, S_2 should be turned on at t_1, which can realize its soft switching. These two steps are similar to the control of a phase-shift-full-bridge, but not exactly the same, as the cascade loads are different. Before S_3 is turned off, S_4 is turned on at t_2, and this state is forbidden in the traditional control. However, precisely because of that, the shoot-through state is provided, which allows the q-Zsource to boost voltage, and different boost factors can be achieved by adjusting the interval between t_2 and t_3. It is noticeable here that the equivalent switching frequency viewed from the q-Zsource is two times the operating frequency of the H Bridge, which greatly reduces the volume and weight of the inductors and capacitors existed in q-Zsource. In addition, the lagging leg (S_3, S_4) is turned off with soft switching, but turned on with hard switching, which lowers the efficiency and needs to be further studied.
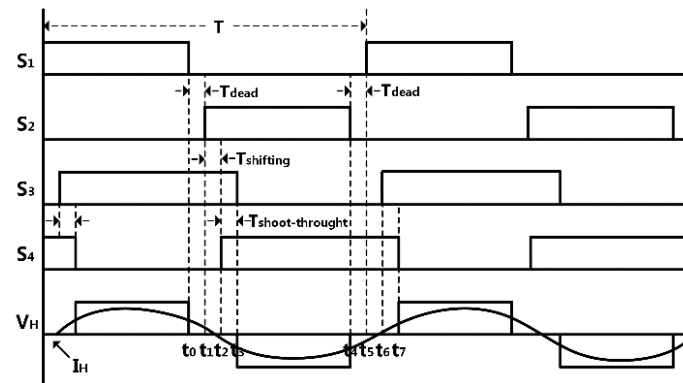
Figure 9. q-Zsource based voltage boost control sequences.

The transmitter and receiver in Figure 6 are high order resonant filters, which only allow the power signals at resonant frequency to pass through. Thus we should evaluate the fundamental components of the waves produced by the H Bridge. The FFT series of square waves depicted in Figure 10 is given as:

$$V = \sum_{n=1,2,3...}^{\infty} \frac{2A}{n\pi} \left[\cos \frac{n\pi T_{non-effective}}{T} - \cos n\pi (1 - \frac{T_{non-effecitve}}{T}) \right] \sin n\omega_r t \tag{18}$$

where A, n, $T_{non-effective}$ and T represent the amplitude of the square wave, harmonic order, non-effective time and cycle time, respectively, and $\omega_r = 2\pi/T$ is the system angular frequency. According to Equation (15), A is actually determined by BF, and $T_{non-effective}$ is determined by T_{dead}, $T_{shifting}$ and $T_{shoot-through}$. Thus the output voltage produced by the H Bridge can be regulated by controlling these parameters appropriately, whereas the voltage stress across the power switches needs to be considered before designing the BF parameter.

The degree of approximation between the square wave shown in Figure 10 and a quasi-sinusoidal wave can be quantified by THD, and the lower the THD, the less the harmonic loss. The THD of the square wave consisted of different non-effective times can be calculated according to Equation (19), where V_n represents the different harmonic amplitudes:

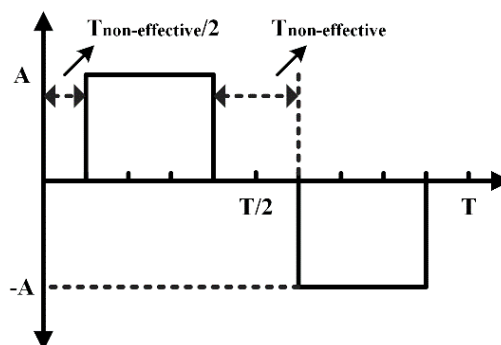$$THD = \frac{\sqrt{\sum_{n=2,3,4...}^{\infty} V_n^2}}{V_1} \tag{19}$$

Figure 10. Typical square wave produced by the H Bridge.

The corresponding THD calculation results at different frequencies are shown in Figure 11, which clearly indicates that the lowest THD happens around 2 μs~3 μs non-effective times at 50 kHz and 1 μs~2 μs non-effective times at 80 kHz, rather than 0 μs non-effective time. The optimal non-effective time is where THD has the smallest decrease with the increasing frequencies. Because we adopt 80 kHz as the system operating frequency, the non-effective time should be designed around 1 μs~2 μs to reduce THD as well as harmonic loss.
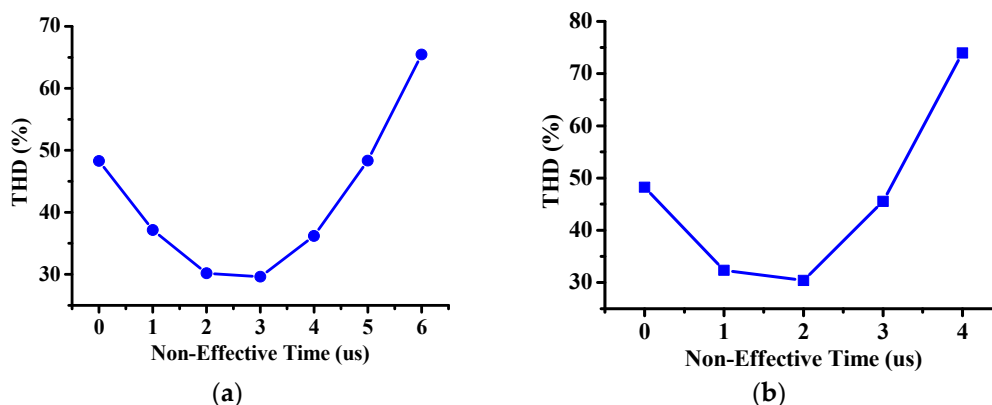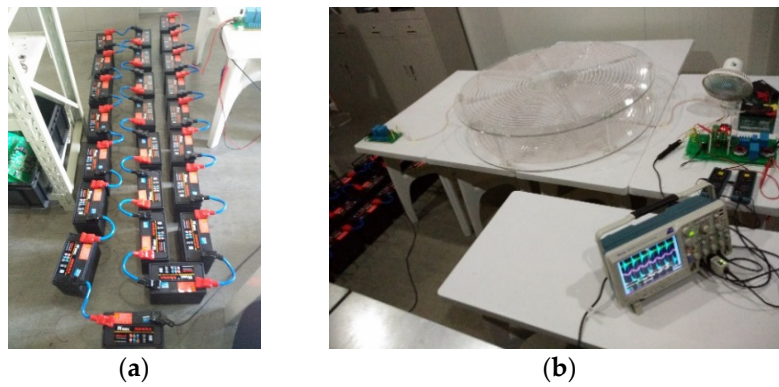

(**a**)   (**b**)

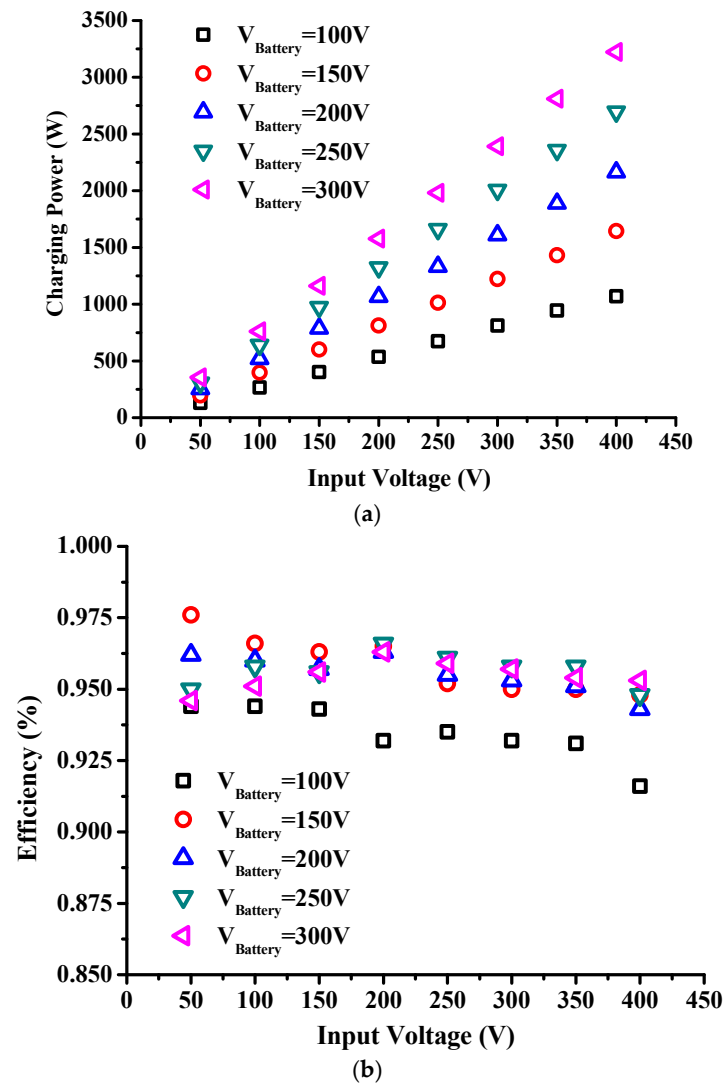**Figure 11.** THDs of square waves with different non-effective times at 50 kHz (**a**) and 80 kHz (**b**).

4. Experiments

A prototype was implemented to validate our research results, as shown in Figure 12, and the magnetic coils are designed based on the nested three-layer optimization method, which will be discussed in our other papers. The prototype is fabricated according to the schematic shown in Figure 6, where the power source adopts a 62100H-600 high-voltage DC power supply (Chroma, Taoyuan, Taiwan), the H Bridge employs four SPW47N60C3 MOSFETs (Infineon, Neubiberg, Germany), the resonant capacitors adopt B32672L thin-film series (TDK-EPCOS, Tokyo, Japan) ,the rectifier consists of four IDW30E65D1 fast recovery diodes (Infineon, Neubiberg, Germany) and the battery pack consists of 24 lead-acid battery units.

Figure 13 shows the transfer characteristics of the wireless power transfer system at 20 cm transfer distance, and it is worth mentioning that the q-Zsource does not work, and is only present as a filter. In Figure 13a, the transfer power increases with rising input voltages or battery pack voltages. In practice, the power factor correction (PFC) with 400 V output voltage is employed to enhance AC power quality, and the 300 V battery pack is widely used for many production-ready vehicles, like Toyota Prius, Chevrolet Volt, Mitsubishi i-MiEV as well as Nissan Leaf, thus we define this situation as the system rated operating state. In the rated state, the charging power is 3220 W as shown in Figure 13a, which is a little bigger than 3 kW, since the battery pack voltage increases from 300 V to 309.7 V when the charging current (RMS value is 10.4 A as shown in Figure 14) flows through the battery resistance, causing an extra voltage drop. Figure 13b shows that the transfer efficiencies are nearly unchanged despite the increasing input voltages or battery pack voltages, and the rated efficiency where the input voltage equals 400 V and the battery pack voltage equals 300 V is around 95%.
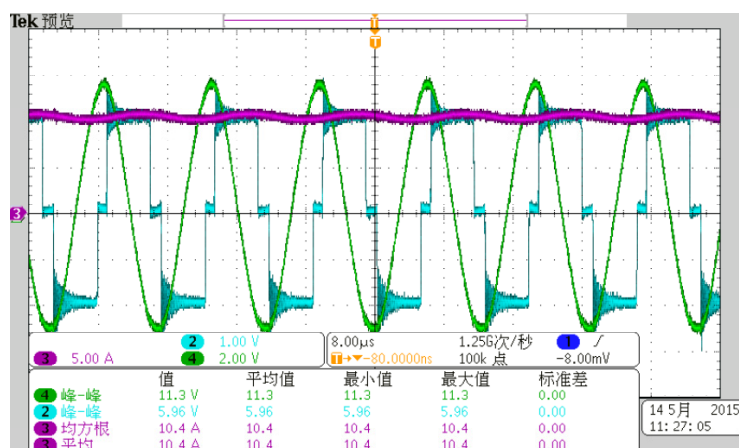
(**a**)   (**b**)

Figure 12. Prototype of wireless power transfer system.   (**a**) 300V lead-acid battery pack. (**b**) Transmitter and receiver of wireless power transfer system. The magnetic coil is placed on the top of a perspex plate and fixed by eight perspex bars.
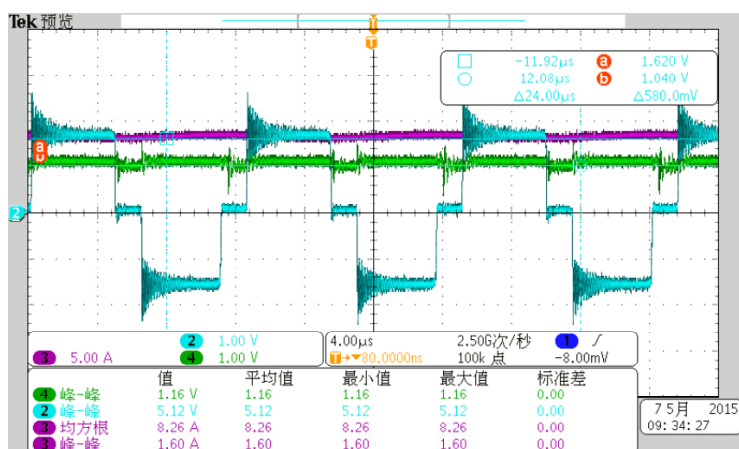

(**a**)

(**b**)

Figure 13. Wireless transfer power (**a**) and efficiency (**b**) at different input voltages and battery pack voltages at 20 cm transfer distance.

Figure 14 shows some critical waveforms of the wireless power transfer system, where the cyan curve shows the output voltage produced by the H Bridge, the green curve shows the voltage across the resonant capacitor in the transmitter and the purple curve shows the charging current for the battery pack. Because the reduction scale of high voltage probe is 200, the measured voltages need to be multiplied by 200. The amplitude of the square-wave voltage produced by the H Bridge is 400 V. The RMS value of the charging current is 10.4 A, and there are some ripple waves, the amplitude of which depends on the filter capacitors. The bigger the filter capacitors, the smaller the ripple waves.
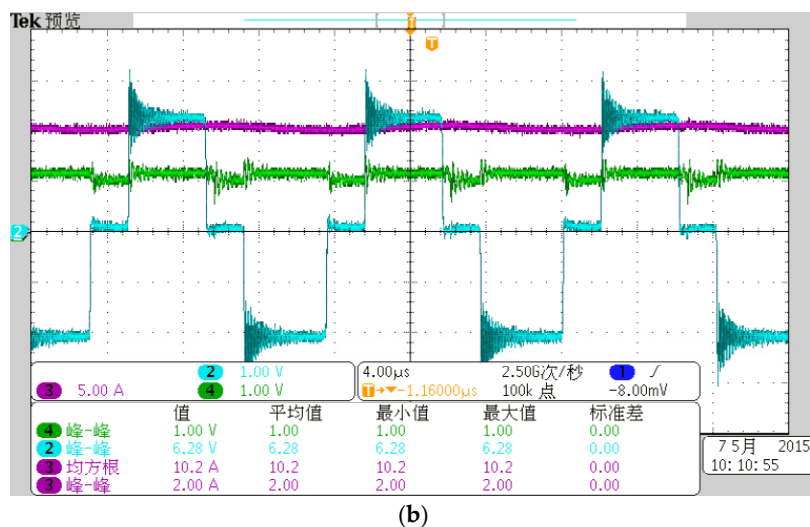

Figure 14. Purple curve: the charging current for the battery pack; cyan curve: the output voltage produced by the H Bridge; green curve: the voltage across the resonant capacitor in the transmitter. They are measured when the system works in the rated state (V_{in} = 400 V, V_B = 309.7 V, $P_{charging}$ = 3220 W, $D_{transfer}$ = 20 cm).

The following experimental results are measured when the q-Zsource works, and two different shoot-through times are shown to clearly demonstrate the q-Zsource principle. Figure 15 indicates that different shoot-through times determine different boost factors. Although the input voltages (green curve) of both Figure 15a,b are identical (200 V), their output voltages (cyan curve) are different. When the shoot-through time is 1 μs, the boost factor is around 1.5, thus the output voltage is around 300 V, and the charging current is 8.26 A. When the shoot-through time is 1.5 μs, the boost factor is around 2, thus the output voltage is around 400 V, and the charging current is 10.2 A. Summarily, the charging currents can be adjusted by controlling the shoot-through times.
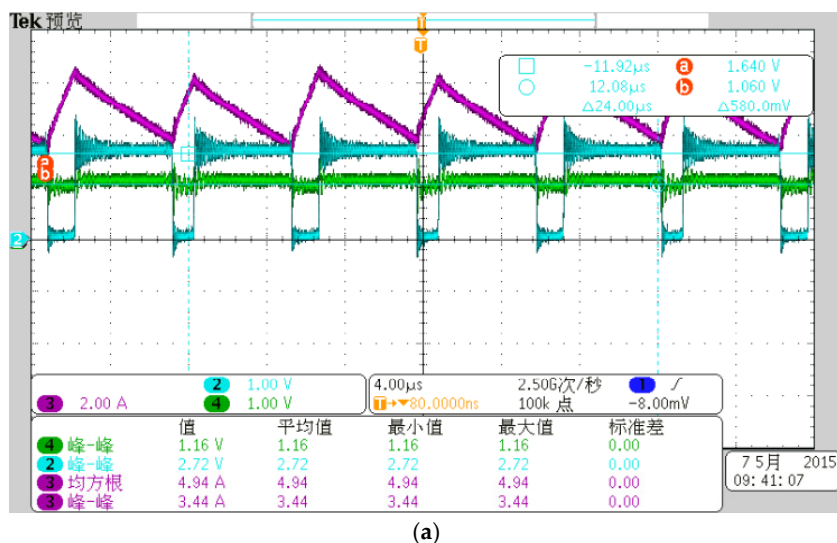

(a)

Figure 15. *Cont.*

(**b**)

Figure 15. Purple curve: the charging currents for the battery pack; green curve: the input voltage of the q-Zsource; cyan curve: the output voltage produced by the H Bridge measured (**a**) at the 1 μs shoot-through time; and (**b**) at the 1.5 μs shoot-through time.

In Figure 16a,b the q-Zsource input voltages (green curve) are the same, but their output voltages (cyan curve) are different due to the different boost factors. Unlike the square-wave voltages produced by the H Bridge, the q-Zsource output voltages are pulsatile and always positive. In the shoot-through state, where the q-Zsource output voltage equals zero, the q-Zsource input current (purple curve) increases with a positive slope. However, it decreases with a negative slope when the q-Zsource enters into the non-shoot-through state.

Figure 17 shows the output currents (purple curve) and voltages (cyan curve) produced by the H Bridge, which validate that the system is basically in the resonant state. However, the quasi-resonant state is not beneficial for soft-switching, and hence, efficiency improvement. In practice, the current produced by the H Bridge should lag the voltage to a certain degree, thus an additional 1 nF capacitor is added into the transmitter capacitor array in this paper. The green curve represents the voltage across the q-Zsource capacitor (C_2 in Figure 6), and it is smaller than the output voltage produced by the H Bridge, but it is bigger than the input voltage of the q-Zsource shown in Figure 16.
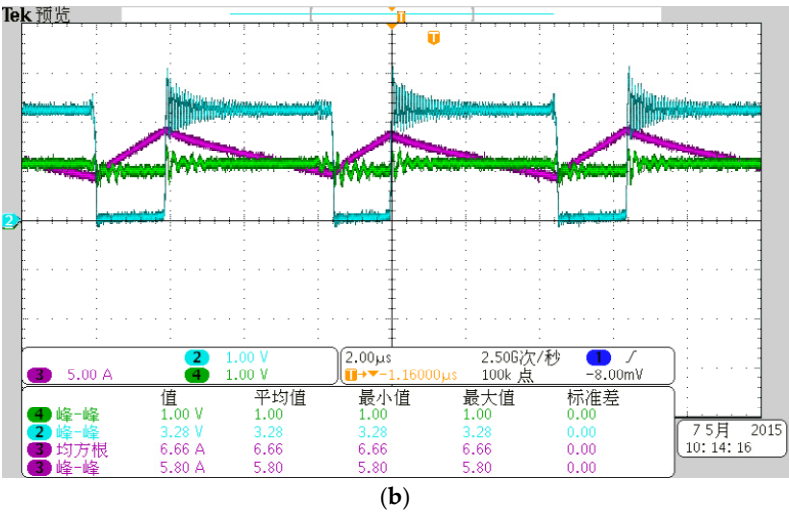

(**a**)

Figure 16. *Cont*.

(**b**)

Figure 16. Purple curve: the input current of q-Zsource, green curve shows the input voltage of q-Zsource, cyan curve shows the output voltage of q-Zsource measured (**a**) at the 1 μs shoot-through time; and (**b**) at the 1.5 μs shoot-through time.
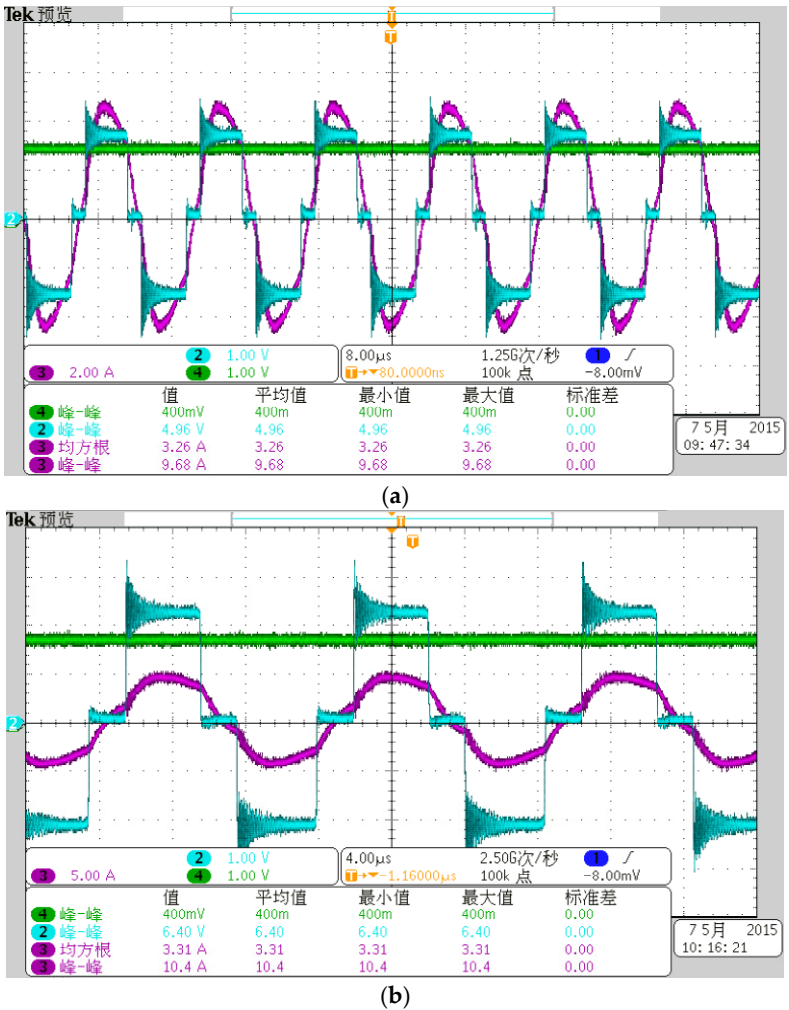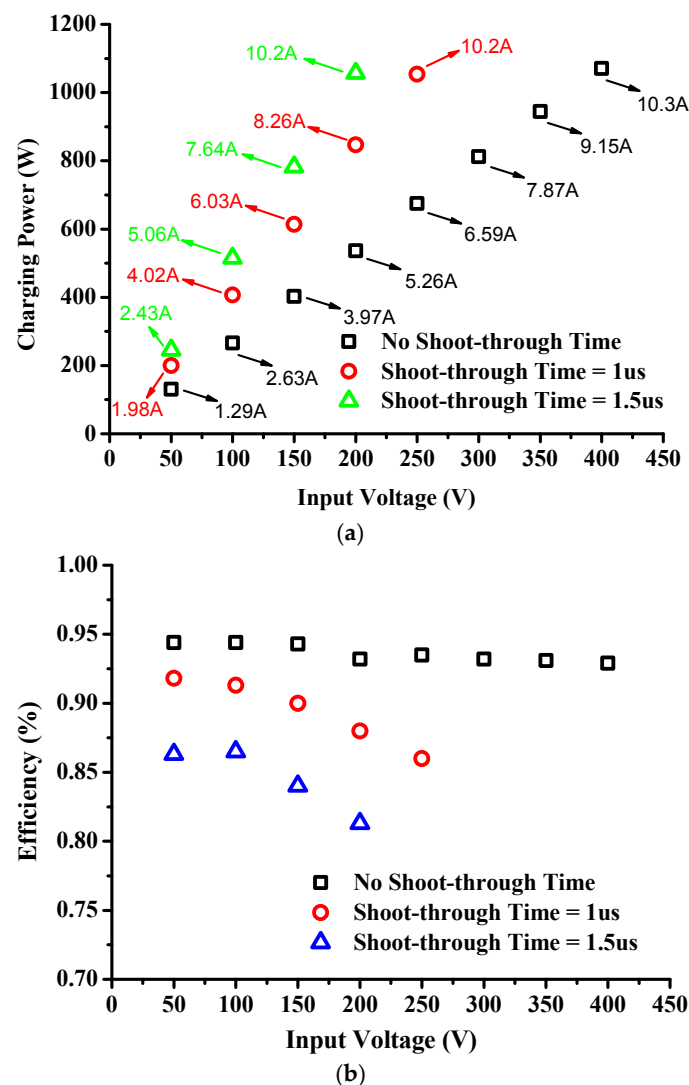

(**a**)

(**b**)

Figure 17. Purple curve: the currents produced by the H Bridge; cyan curve: the output voltages produced by the H Bridge; green curve: the capacitor voltages of the q-Zsource measured (**a**) at the 1 μs shoot-through time; and (**b**) at the 1.5 μs shoot-through time.

Figure 18a indicates that the charging power or current can be adjusted by changing the shoot-through times. Take the 200 V input voltage as an example, the charging current is 5.26 A when there is no shoot-through time, and it is increased to 8.26 A with 1 μs shoot-through time, and it is further increased to 10.2 A when the shoot-through time is 1.5 μs. Because the boost factor is close to 2 at 1.5 μs shoot-through time, the input voltages above 200 V are not allowed, which may damage the resonate capacitors. In Figure 18b, the efficiencies decline with the increasing shoot-through times, for the shoot-through state makes the MOSFETs of latter bridge arm lost their soft-switching conditions. Additionally, the operating frequency (160 kHz) of q-Zsource doubles that (80 kHz) of wireless power transfer system, which further causes the decline in the transfer efficiency. This phenomenon can be suppressed by reducing the operating frequency of q-Zsouce. If it is decreased to 40 kHz, the loss can be theoretically reduced as much as four times. However, the reduction of the frequency requires bigger inductors and capacitors than before, thus the q-Zsource parameters need to be re-optimized, which is our future work.

(a)

(b)

Figure 18. Wireless transfer power (**a**) and efficiency (**b**) characteristics based on the q-Zsource voltage boosting method at 20 cm transfer distance.

5. Conclusions

This paper studies a 3 kW vehicle-mounted wireless power transfer system. First, the efficiency of the LC-LC series topology is verified to be higher than that of the LCL-LCL topology when their

transfer power are the same. Then a q-Zsource-based power regulation method is proposed to adjust the charging current online. At last, a 3 kW prototype with ~95% efficiency over a 20 cm transfer distance is implemented to validate our research results. Different shoot-through time durations determine different charging currents despite the same input voltage. When the input voltage is set to be 200 V, a 1 µs shoot-through time can boost the charging current from 5.26 A to 8.26 A, and a 1.5 µs shoot-through time can boost the charging current from 5.26 A to 10.2 A. We hope the work presented in this paper is beneficial to the development of wireless power transfer systems.

Author Contributions: Zhenshi Wang designed the system and analyzed the results, Xuezhe Wei and Haifeng Dai provided guidance and key suggestions.

Conflicts of Interest: The authors declare no conflict of interest.

References

1. Brown, W.C. The history of power transmission by radio waves. *IEEE Trans. Microwave Theory Tech.* **1984**, *32*, 1230–1242. [CrossRef]
2. Tucker, C.A.; Warwick, K.; Holderbaum, W. A contribution to the wireless transmission of power. *Int. J. Electr. Power Energy Syst.* **2013**, *47*, 235–242. [CrossRef]
3. Brown, W.C. Status of the microwave power transmission components for the solar power satellite (SPS). *IEEE MTT-S Int. Microwave Symp. Dig.* **1981**, *81*, 270–272.
4. Glaser, P.E. Power from the Sun: Its future. *Science* **1968**, *162*, 857–861. [CrossRef] [PubMed]
5. Covic, G.A.; Boys, J.T. Modern trends in inductive power transfer for transportation applications. *IEEE J. Emerg. Sel. Top. Power Electr.* **2013**, *1*, 28–41. [CrossRef]
6. Wei, X.Z.; Wang, Z.S.; Dai, H.F. A critical review of wireless power transfer via strongly coupled magnetic resonances. *Energies* **2014**, *7*, 4316–4341. [CrossRef]
7. Kurs, A.; Karalis, A.; Moffatt, R.; Joannopoulos, J.D.; Fisher, P.; Soljacic, M. Wireless power transfer via strongly coupled magnetic resonances. *Science* **2007**, *317*, 83–86. [CrossRef] [PubMed]
8. Sample, A.P.; Meyer, D.A.; Smith, J.R. Analysis, experimental results, and range adaptation of magnetically coupled resonators for wireless power transfer. *IEEE Trans. Ind. Electron.* **2011**, *58*, 544–554. [CrossRef]
9. Li, X.H.; Zhang, H.R.; Peng, F.; Li, Y.; Yang, T.Y.; Wang, B.; Fang, D. A wireless magnetic resonance energy transfer system for micro implantable medical sensors. *Sensors* **2012**, *12*, 10292–10308. [CrossRef] [PubMed]
10. Puccetti, G.; Stevens, C.J.; Reggiani, U.; Sandrolini, L. Experimental and numerical investigation of termination impedance effects in wireless power transfer via metamaterial. *Energies* **2015**, *8*, 1882–1895. [CrossRef]
11. Sun, L.; Tang, H.; Zhang, Y. Determining the frequency for load-independent output current in three-coil wireless power transfer system. *Energies* **2015**, *8*, 9719–9730. [CrossRef]
12. Sanghoon, C.; Yong-Hae, K.; Kang, S.-Y.; Myung-Lae, L.; Jong-Moo, L.; Zyung, T. Circuit-model-based analysis of a wireless energy-transfer system via coupled magnetic resonances. *IEEE Trans. Ind. Electron.* **2011**, *58*, 2906–2914.
13. Kiani, M.; Uei-Ming, J.; Ghovanloo, M. Design and optimization of a 3-coil inductive link for efficient wireless power transmission. *IEEE Trans. Biomed. Circuits Syst.* **2011**, *5*, 579–591. [CrossRef] [PubMed]
14. Dukju, A.; Songcheol, H. A study on magnetic field repeater in wireless power transfer. *IEEE Trans. Ind. Electron.* **2013**, *60*, 360–371.
15. Musavi, F.; Eberle, W. Overview of wireless power transfer technologies for electric vehicle battery charging. *IET Power Electron.* **2014**, *7*, 60–66. [CrossRef]
16. Del Toro, T.G.X.; Vázquez, J.; Roncero-Sanchez, P. Design, implementation issues and performance of an inductive power transfer system for electric vehicle chargers with series-series compensation. *IET Power Electron.* **2015**, *8*, 1920–1930.
17. Siqi, L.; Mi, C.C. Wireless power transfer for electric vehicle applications. *IEEE J. Emerg. Sel. Top. Power Electron.* **2015**, *3*, 4–17. [CrossRef]

18. Keeling, N.A.; Covic, G.A.; Boys, J.T. A unity-power-factor IPT pickup for high-power applications. *IEEE Trans. Ind. Electron.* **2010**, *57*, 744–751. [CrossRef]

19. Hwang, S.-H.; Kang, C.G.; Son, Y.-H.; Jang, B.-J. Software-based wireless power transfer platform for various power control experiments. *Energies* **2015**, *8*, 7677–7689. [CrossRef]

20. Zaheer, A.; Covic, G.A.; Kacprzak, D. A bipolar pad in a 10-kHz 300-W distributed IPT system for AGV applications. *IEEE Trans. Ind. Electron.* **2014**, *61*, 3288–3301. [CrossRef]

21. Madawala, U.K.; Thrimawithana, D.J. New technique for inductive power transfer using a single controller. *IET Power Electron.* **2012**, *5*, 248–256. [CrossRef]

22. Gao, Y.; Farley, K.; Tse, Z. A uniform voltage gain control for alignment robustness in wireless EV charging. *Energies* **2015**, *8*, 8355–8370. [CrossRef]

23. Chwei-Sen, W.; Covic, G.A.; Stielau, O.H. Power transfer capability and bifurcation phenomena of loosely coupled inductive power transfer systems. *IEEE Trans. Ind. Electron.* **2004**, *51*, 148–157.

24. Ricketts, D.S.; Chabalko, M.J.; Hillenius, A. Experimental demonstration of the equivalence of inductive and strongly coupled magnetic resonance wireless power transfer. *Appl. Phys. Lett.* **2013**, *102*, 053904. [CrossRef]

25. Birrell, S.A.; Wilson, D.; Yang, C.P.; Dhadyalla, G.; Jennings, P. How driver behaviour and parking alignment affects inductive charging systems for electric vehicles. *Transp. Res. C Emerg. Technol.* **2015**, *58*, 721–731. [CrossRef]

26. Choi, W.P.; Ho, W.C.; Liu, X.; Hui, S.Y.R. Comparative study on power conversion methods for wireless battery charging platform. In Proceedings of the 2010 14th International Power Electronics and Motion Control Conference (EPE/PEMC), Ohrid, Macedonia, 6–8 September 2010; pp. S15:9–S15:16.

27. Xuan, N.B.; Vilathgamuwa, D.M.; Foo, G.H.B.; Peng, W.; Ong, A.; Madawala, U.K.; Trong, D.N. An Efficiency Optimization Scheme for Bidirectional Inductive Power Transfer Systems. *IEEE Trans. Power Electron.* **2015**, *30*, 6310–6319.

28. Jun-Young, L.; Byung-Moon, H. A Bidirectional Wireless Power Transfer EV Charger Using Self-Resonant PWM. *IEEE Trans. Power Electron.* **2015**, *30*, 1784–1787.

29. Madawala, U.K.; Thrimawithana, D.J. A Bidirectional Inductive Power Interface for Electric Vehicles in V2G Systems. *IEEE Trans. Ind. Electron.* **2011**, *58*, 4789–4796. [CrossRef]

30. Madawala, U.K.; Thrimawithana, D.J. Modular-based inductive power transfer system for high-power applications. *IET Power Electron.* **2012**, *5*, 1119–1126. [CrossRef]

31. Xuan, N.B.; Foo, G.; Ong, A.; Vilathgamuwa, D.M.; Madawala, U.K. Efficiency optimization for bidirectional IPT system. In Proceedings of the 2014 IEEE Transportation Electrification Conference and Expo (ITEC), Dearborn, MI, USA, 15–18 June 2014; pp. 1–5.

32. Madawala, U.K.; Thrimawithana, D.J. Current sourced bi-directional inductive power transfer system. *IET Power Electron.* **2011**, *4*, 471–480. [CrossRef]

33. Zheng, P.F. Z-source inverter. *IEEE Trans.Ind. Appl.* **2003**, *39*, 504–510. [CrossRef]

34. Peng, F.X.; Guang, W.X.; Qiao, C.Z. A single-phase AC power supply based on modified Quasi-Z-Source Inverter. *IEEE Trans. Appl. Supercond.* **2014**, *24*, 1–5. [CrossRef]

35. Boys, J.T.; Covic, G.A. Decoupling Circuits. U.S. 7279850B2, 9 October 2005.

36. Hothongkham, P.; Kongkachat, S.; Thodsaporn, N. Performance comparison of PWM and phase-shifted PWM inverter fed high-voltage high-frequency ozone generator. In Proceedings of the 2011 IEEE Region 10 Conference on Convergent Technologies for the Asia-Pacific Region, Bali, Indonesia, 21–24 November 2011; pp. 976–980.